Catalysis Today 418 (2023) 114132

Contents lists available at ScienceDirect

Catalysis Today

journal homepage: www.elsevier.com/locate/cattod

Design and photo-Fenton performance of Graphene/CuS/Fe_3O_4 tertiary nanocomposites for Rhodamine B degradation

Renata Matos [a], Iwona Kuźniarska-Biernacka [a,*], Mariana Rocha [a,1], João H. Belo [b], João Pedro Araújo [b], Ana C. Estrada [c], Joana L. Lopes [c], Tushti Shah [d], Brian A. Korgel [d], Clara Pereira [a], Tito Trindade [c], Cristina Freire [a,*]

[a] REQUIMTE/LAQV, Departamento de Química e Bioquímica, Faculdade de Ciências, Universidade do Porto, Rua do Campo Alegre s/n, 4169-007 Porto, Portugal
[b] IFIMUP, Departamento de Física e Astronomia da Faculdade de Ciências da Universidade do Porto, Rua do Campo Alegre, 687, 4169-007 Porto, Portugal
[c] Departamento de Química e CICECO, Universidade do Aveiro, 3810-193 Aveiro, Portugal
[d] McKetta Department of Chemical Engineering and Texas Materials Institute, The University of Texas at Austin, Austin, TX 78712, USA

ARTICLE INFO

Keywords:
Graphene flakes
Graphene hybrid nanostructures
Iron oxide nanoparticles
Copper sulfide nanocrystals
Rhodamine B
Photocatalysis
Adsorption

ABSTRACT

This study describes nanocomposites of graphene flakes (GF) combined with CuS, Fe_3O_4 and CuS−Fe_3O_4 nanoparticles prepared by wet chemical methods. The Fe_3O_4 and/or CuS nanoparticles were directly anchored onto GF without requiring additional chemical treatment. The composition, structure and morphology of the nanocomposites, as well as of the pristine GF and metal oxide/sulfide nanoparticles were characterised by X − ray photoelectron spectroscopy (XPS), Raman spectroscopy, Fourier transform infrared spectroscopy (FTIR), powder X − ray diffraction (XRD) and scanning electron microscopy (SEM) techniques. The results confirmed the successful attachment of CuS nanophases (size range: 23.7–50.1 nm) and/or Fe_3O_4 nanoparticles (size range: 10.6–15.8 nm). The adsorption and photocatalytic properties of the GF−based nanocomposites were evaluated at room temperature using Rhodamine B (RhB) as a model contaminant. Theoretical models were fitted to the adsorption kinetic results using the pseudo-first-order, pseudo-second-order and Elovich equations, while the adsorption mechanism was determined using the intraparticle diffusion, Bangham and Boyd models. The RhB adsorption efficiency was 6.5% for GF@CuS−Fe_3O_4 after 180 min contact time, whereas for the other materials was significantly higher: 97.6%, 60.9% and 31.9% for GF, GF@CuS and GF@Fe_3O_4, respectively. The adsorption capacity of GF and composites fitted the pseudo−second−order kinetic and Elovich models. The influence of the nanostructures composition on the corresponding photocatalytic activity in the degradation of RhB under a 150 W halogen lamp was also evaluated. The GF@CuS−Fe_3O_4 nanocomposite totally eliminated the dissolved RhB after 60 min irradiation, whereas the GF@CuS, GF@Fe_3O_4 and pristine Fe_3O_4 removed 75.6%, 80.9% and 30.8%, respectively, after 180 min irradiation. It was found that the photocatalytic behaviour of the composites was best described by the first−order kinetic model. The rate constant of the photocatalytic RhB removal for GF@CuS−Fe_3O_4 ($k = 7.05 \times 10^{-2}$ min^{-1}) was 2.1, 5.1 and 15.0 times higher than those obtained for GF@CuS, GF@Fe_3O_4 and pristine Fe_3O_4, respectively, after 60 min of visible light irradiation.

1. Introduction

Semiconductor photocatalysis has been widely used as a "green" oxidation technology applied to wastewater treatment normally using mild conditions [1]. Many semiconductor photocatalysts have been studied in the field of photocatalytic degradation of organic dyes, namely metal oxides such as TiO_2 and ZnO [2], Nb_2O_5 [3], Ta_2O_5 [2], among others. However, the technological application of these photocatalysts is limited by their wide band gap (>3 eV) and the requirement of UV light to photogenerate electron−hole pairs.

It should be noted that the UV region comprises nearly 4% of the whole sunlight spectrum, while 45% of the solar energy belongs to

* Corresponding authors.
E-mail addresses: iwonakb@fc.up.pt (I. Kuźniarska-Biernacka), acfreire@fc.up.pt (C. Freire).
[1] Current affiliation: IFIMUP – Instituto de Física de Materiais Avançados, Nanotecnologia e Fotónica, Departamento de Física e Astronomia, Faculdade de Ciências, Universidade do Porto, Rua do Campo Alegre s/n, 4169-007 Porto, Portugal.

https://doi.org/10.1016/j.cattod.2023.114132
Received 16 December 2022; Received in revised form 25 February 2023; Accepted 19 March 2023
Available online 22 March 2023

visible light [3]. Moreover, solar energy is easily accessible and free. Therefore, the development of efficient photocatalysts with a visible light response for wastewater treatment has been an important subject in recent years. Semiconductors with a narrower band gap (1.2–2.2 eV, depending on their stoichiometry and composition), such as distinct crystalline phases of copper sulfides ($Cu_{2-x}S$, $0 < x < 1$), are of great interest for visible light photocatalysis [4]. $Cu_{2-x}S$ nanophases have been synthesized in various morphologies [4,5], such as hollow spheres, rods, tubes, wires and flowers, allowing the nanoengineering of morphological-dependent chemical and physical properties. Herein, we have explored the additional use of magnetite (Fe_3O_4) nanoparticles (band gap = 2.8 eV) [6], which gives the additional benefits of easy magnetic separation of the catalyst from water and the possibility of decomposing pollutants through the photo−Fenton type reactions.

Currently, the attention is directed towards harnessing the outstanding properties of graphene for designing the next−generation of photocatalytic systems with enhanced performance. With the discovery of new chemical routes for the synthesis of monolayer graphene, multilayer graphene and graphene flakes/nanoplatelets, researchers have been actively involved in the immobilization of organic compounds (molecular linkers, proteins) and inorganic nanomaterials (metal nanoparticles, metal oxide semiconductors) onto graphene and its derivatives [7]. Graphene flakes (GF) are stacked atomic layers of carbon with a honeycomb lattice structure. One of the advantages of using GF in these applications is their easier dispersion when compared to both single−layer graphene and carbon nanotubes (CNT) [8–10]. The large surface area, high electron mobility at room temperature, superior mechanical properties and excellent optical transmittance makes graphene an ideal matrix for photocatalyst carriers or promoters [11]. Additionally, GF can be obtained in high yields in comparison with other graphene family networks (single-layer graphene or carbon nanotubes), which is advantageous for composite up-scale fabrication [9,12]. Usually, for such studies, graphene oxide (GO) or reduced GO (rGO) have been used in the nanocomposite formulations. These nanocomposites also include photocatalysts, such as metal oxides (*e.g.*, TiO_2, ZnO, Cu_2O, Fe_2O_3, Mn_2O_3 and WO_3), metal sulfides (*e.g.*, CdS, In_2S_3, Sb_2S_3 and CdSe) and metallates (*e.g.*, $BiVO_4$, Bi_2WO_6 and Bi_2MoO_6) [11,13]. The CuS and Fe_3O_4 nanoparticles attached onto graphene nanoplatelets, modified GO or rGO, have been explored to achieve effective degradation of several organic pollutants [14–18]. The results show that the rGO−Fe_3O_4 composites led to nearly complete degradation of Rhodamine B (87.13%) under light irradiation for 120 min [19]. Whereas GO−CuS provided 41.3–95.4% degradation of Rhodamine B after 90 min irradiation (500 W Xe lamp), depending on the GO:CuS ratio [20]. Nevertheless, three−component photocatalysts composed of high purity GF, CuS and Fe_3O_4 have not been reported yet.

In fact, anchoring metal oxide/sulfide nanoparticles onto pristine graphene without previous oxidation to create oxygen-containing moieties (*e.g.* GO or rGO) seems attractive. This helps retain the purity of graphene, as oxygen-containing functional groups act as impurity components and significantly increase the number of sp^2 −sp^3 bonds. Moreover, their presence modifies the electrical conductivity of graphene, which in turn might reduce the nanocomposite efficiency in applications governed by charge carriers transport, *e.g.* photocatalysis [21]. Pure graphene layers, in turn, increase the charge carrier's lifetime, thus promoting mechanisms for the fast photo−oxidation of organic substrates. In addition, the high available surface area provides an advantage for high adsorption of dye molecules and fast photo−excitation of carriers, respectively [12].

In this study, we report for the first time, the synthesis and properties of the three component GF−based nanocomposite (GF@CuS−Fe_3O_4). Furthermore, the photocatalytic behaviour of the three-component photocatalyst was assessed by using the Rhodamine B (RhB) dye as a water contaminant model, and comparative photocatalytic studies were carried out using GF@Fe_3O_4, GF@CuS and pristine nanoparticles. The GF@Fe_3O_4, GF@CuS and GF@CuS−Fe_3O_4 nanocomposites were fabricated through the combination of two or three different components with complementary roles in order to improve the efficiency and stability of the photocatalysts. The selection of Fe_3O_4 (Fenton−type catalyst), CuS (visible light photocatalyst) and GF (charge carrier) allows a photo−Fenton−type reaction to develop a green, cost−effective and environmentally−friendly way to depollute aqueous effluents. Moreover, the preparation method is easy and can be potentially employed to synthesize large−scale batches of photocatalysts.

2. Experimental

2.1. Materials

Commercial GF were purchased from Graphene Technologies (Lot #GTX−7/6–10.4.13). 1–amine− 2–propanol (93%, MIPA), acetone (analytical grade), RhB (>95% HPLC grade), potassium bromide (≥99%, FT−IR grade), hydrogen peroxide 30 wt% in H_2O (ACS reagent), copper diethyldithiocarbamate (≥97%) and ethylenediamine were acquired from Sigma−Aldrich. Iron(II) chloride tetrahydrate (99.0%, analytical grade) was obtained from Fluka and absolute ethanol (analytical grade) from Fisher Chemicals. Iron(III) chloride hexahydrate (98%, analytical grade) was obtained from Merck, and hydrochloric acid (37%, analytical grade) was purchased from Panreac. Ultrapure water (Millipore, specific resistivity 18 MΩ·cm) was used throughout the experiments. All reagents were used without further purification.

2.2. Physicochemical characterization

X − ray diffraction (XRD) analyses were performed at "IFIMUP, Departamento de Física e Astronomia da Universidade do Porto" (Portugal) on a Rigaku Smartlab diffractometer. The XRD measurements were performed at room temperature over the range $2\theta = 15 - 80^{\circ}$ using Cu Kα radiation ($\lambda = 1.5406$ Å) and the Bragg−Brentano $\theta/2\theta$ configuration. The X-ray diffractograms refinements were performed by the Whole Powder Pattern Fitting (WPPF) method and the different crystalline phase fractions were estimated by the Reference Intensity Ratio (RIR) method.

The FTIR spectra were obtained in KBr pellets containing 0.2 wt% material, using a Jasco FT−IR 460 Plus spectrometer. All spectra were collected at room temperature, in the 4000 − 400 cm^{-1} range using a resolution of 4 cm^{-1} and 32 scans.

Raman spectra were collected using a Witec micro-Raman spectrometer Alpha 300 with a 532 nm (5 mW) incident laser light and a 20 × objective lens. The graphene samples were deposited on a glass slide for spectroscopy. For each sample, multiple spectra were collected.

X − ray photoelectron spectroscopy (XPS) was performed at "Centro de Materiais da Universidade do Porto" (CEMUP, Portugal), in a Kratos Axis Ultra HSA spectrometer. All the materials were compressed into pellets before the XPS studies. To correct possible deviations caused by the electric charge of the samples, the C 1 s line at 284.6 eV was taken as the internal standard. XPS spectra were deconvoluted with CasaXPS 2.3.12 software, using non-linear least squares fitting routine after a Shirley-type background subtraction and the peaks were interpreted using a combination of Gaussian/Lorentzian functions.

Scanning electron microscopy (SEM) and energy-dispersive X-ray spectroscopy (EDS) studies were performed at CEMUP (Portugal), using a high−resolution environmental scanning electron microscope FEI Quanta 400 FEG ESEM at 15 kV equipped with energy−dispersive X − ray spectrometer EDAX Genesis X4M.

Ultraviolet−visible (UV−Vis) spectra were registered on a Varian Cary50Bio spectrophotometer, in the range of $\lambda = 650–200$ nm, using a quartz cell with a 1 cm path length.

Atomic absorption spectroscopy (AAS) was performed on a Thermo Scientific ICE 3300 spectrometer, to determine the eventual metal leaching from the catalyst to the reaction medium during the catalytic tests.

Zeta potential measurements were performed at 25 °C on a Microtrac Intruments-Zetatrac 173 apparatus.

Proton nuclear magnetic resonance (^{1}H NMR) spectra of the as-prepared RhB solution and the reaction media after the photocatalytic tests were acquired in the 0–10 ppm range at "Laboratório de Análise Estrutural", CEMUP (Portugal) using a Bruker Advance III 400 spectrometer operating at 400.15 MHz for ^{1}H atoms, equipped with pulse gradient units, capable of producing magnetic field pulsed gradients in the z − direction of 50.0 G cm^{-1}. The samples for NMR analysis were prepared using the following methodology: 50 mL of remaining solution (filtered) after the photocatalytic tests were dried under reduced pressure at 45 °C using a rotary evaporator and the resulting residue was dissolved in 2 mL dimethyl sulfoxide−d_6.

Measurements of the magnetic properties of the materials were investigated by using a commercial Quantum Design MPMS3 SQUID magnetometer. The magnetization (M) as a function of the applied magnetic field (H) measurements were performed at 300 K for a maximum H of 50 kOe.

2.3. (Photo)catalysts preparation

2.3.1. Synthesis of Fe_3O_4

The synthesis of Fe_3O_4 nanoparticles was performed by coprecipitation under an inert atmosphere, described in detail elsewhere [22]. Briefly, 2 mmol of $FeCl_3{\cdot}6\ H_2O$ and 1 mmol of $FeCl_2{\cdot}4\ H_2O$ were dissolved in 25 mL of 0.5 M HCl solution. This solution was added to 200 mL of 3.0 M MIPA solution under vigorous mechanical stirring. A black precipitate formed immediately, and the reaction was maintained under mechanical stirring for 2 h at room temperature. After that time, the precipitate was magnetically separated and washed with ultrapure water several times and acetone once. The solid was dried at room temperature under reduced pressure.

2.3.2. Preparation of GF@Fe_3O_4

The GF@Fe_3O_4 nanocomposite was prepared in the following way: 0.9 mmol of $FeCl_2{\cdot}4\ H_2O$ were dissolved in 5 cm^3 of 0.5 M HCl and 1.8 mmol of $FeCl_3{\cdot}6\ H_2O$ were dissolved in 15 mL of Millipore water. The two solutions were mixed and then added to 50 mg of GF and the resulting mixture was sonicated and placed under mechanical stirring for 1 h to promote the complete adsorption of the salts onto the graphene material. Then, the dispersion was added to a solution of 100 mL of 3.0 M MIPA the, which was maintained under vigorous mechanical stirring for 2 h at room temperature under inert conditions. After that time, the resulting material was magnetically separated, washed with ultrapure water several times and a final wash with acetone. The solid was dried under reduced pressure at room temperature.

2.3.3. Preparation of CuS

Copper sulfide nanophases were obtained by the thermolysis of copper diethyldithiocarbamate precursor, ($Cu[S_2CN(C_2H_5)_2]_2$) [23]. Hence, ethylenediamine (9 mmol) was added to 25 mL of an ethanolic solution containing $Cu[S_2CN(C_2H_5)_2]_2$ (58 μmol), and the mixture was refluxed for 1 h. The dark solid formed was isolated, washed with ethanol, and kept under N_2.

2.3.4. Preparation of GF@CuS

The GF sheets were decorated with copper sulfide nanophases according to the procedure described in ref. [24]. In a typical experiment, ethylenediamine (9 mmol) was added to a dry ethanol suspension of GF (20 mg, 25 mL) containing the metal precursor (58 μmol). The mixture was stirred at reflux temperature until a color change of the reaction mixture was observed. The hybrid nanostructure was collected by centrifugation (6000 rpm, 15 min), washed with ethanol and dried at room temperature under N_2.

2.3.5 Preparation of GF@CuS−Fe_3O_4.

The experimental procedure for the preparation of the magnetic−photocatalytic graphene nanocomposites was similar to that used to prepare the GF@Fe_3O_4 and GF@CuS nanocomposites described in 2.3.2 and 2.3.4, respectively. Briefly, 0.9 mmol of $FeCl_2{\cdot}4\ H_2O$ and 1.8 mmol of $FeCl_3{\cdot}6\ H_2O$ were dissolved in 5 cm^3 of 0.5 M HCl and in 15 mL of Millipore water, respectively. The two solutions were mixed and then added to 50 mg of GF@CuS. The resulting mixture was sonicated and mechanicaly stirred for 1 h. After that time, the dispersion was added to a solution of 100 mL of 3.0 M MIPA, under mechanical stirring for 2 h at room temperature under inert conditions. The resulting material (GF@CuS−Fe_3O_4) was magnetically separated, washed with ultrapure water several times and a final wash with acetone. The solid was dried under reduced pressure at room temperature.

2.4. Adsorption and photocatalytic performance tests

The adsorption properties and photocatalytic activity of the obtained nanomaterials were evaluated using RhB as a model compound. The adsorption experiments were carried out by stirring 20 mg of catalyst with 200 mL aqueous RhB solution (5.8 mg L^{-1}) at 200 rpm for 180 min. The samples were collected at fixed time intervals and analysed by UV−Vis spectroscopy. The amount of adsorbed RhB *per* gram of adsorbent, adsorption capacity (uptake, q (mg g^{-1})), was calculated according to the following equation:

$$q = \frac{V(C_0 - C_e)}{W} \quad (1)$$

where C_0 and C_e are the initial and equilibrium concentrations of RhB (mg L^{-1}), respectively, V is the volume of the solution (L), and W is the mass of the adsorbent (g).

The percentage of RhB uptake by the sorbent (sorption efficiency) was calculated using the following equation:

$$\text{Sorption efficiency} = \frac{C_0 - C_f}{C_0} \times 100 \quad (2)$$

where C_0 is the initial concentration of RhB in the solution (mg L^{-1}) and C_f is the concentration of RhB in the solution (mg L^{-1}) after 180 min of contact. In order to determine which mechanism is the rate−determining step, the kinetic studies were analysed using six kinetic models including first−order [25], the McKay and Ho pseudo−second order [26], Weber−Morris intraparticle diffusion [27], Elovich [28,29], Bangham [30,31] and Boyd [32,33] The respective equations (eqs. S1–S7) are presented in the Supplementary Material.

The photocatalytic activity of the obtained nanomaterials was evaluated after the adsorption studies, under similar experimental conditions to those used in the adsorption tests, but in the presence of H_2O_2 and light irradiation. The light source was a 150 W halogen lamp (Osram), the emission spectum is presented in Fig. S1 the Supplementary Material. A general procedure was carried out as follows: firstly, 200 mL aqueous RhB solution (5.8 mg L^{-1}) was placed in a water−jacketed reactor. Then, 20 mg of catalyst was dispersed in the RhB solution and 1 mL of H_2O_2 was added. The suspension was stirred in the dark for 180 min to achieve the adsorption–desorption equilibrium. Then, the visible light was turned on for the photocatalytic degradation experiments. Samples were withdrawn periodically from the reactor, then centrifuged and analysed by UV−Vis spectroscopy. The photocatalytic efficiency of the materials was measured by C/C_0, where C_0 and C are the RhB concentrations at $t = 0$ min and any reaction time t (min), respectively. The concentration of the RhB dye was calculated by a standard curve (Fig. S1 in the Supplementary Material), using the value of maximum absorbance of RhB in water at $\lambda = 553$ nm. The reproducibility of the results was checked by repeating the results at least two times and was found to be within acceptable limits (<1%). The blank experiments were performed in the absence of the photocatalysts in the presence/absence of H_2O_2 under light irradiation. After the catalytic test, the most promising catalyst was magnetically-separed with an

external magnet, washed with water and ethanol, dried under vacuum and tested in subsequent cycles under the same experimental conditions.

3. Results and discussion

3.1. Materials characterization

The XRD patterns of GF, pristine Fe_3O_4, CuS and GF nanocomposites are presented in Fig. 1. The diffraction peak located at $2\theta = 26.2°$ predominates in the XRD pattern of GF, which corresponds to the (002) reflection of graphite. Moreover, the peaks at $2\theta = 42.8°$ and 53.7° are assigned to (100) and (004) reflections, respectively [34]. The XRD pattern of CuS shows broad diffraction peaks at $2\theta = 29.3$, 31.8, 32.8, 47.8, 48.0, 52.71 and 59.3º, which are respectively assigned to the (102), (103), (006), (107), (110), (108) and (116) reflections of CuS (covellite, ICDDPDF nº 00–006–0464) [35]. The diffraction peaks observed in the diffractogram of the GF@CuS hybrid correspond to the (102), (103), (006) and (110) crystalline planes of the hexagonal structure of CuS, which clearly confirms the presence of this semiconductor on the GF sheets. The XRD pattern of the as-prepared Fe_3O_4 nanoparticles present peaks at $2\theta = 18.0°$, 30.0°, 35.4°, 43.2°, 53.5°, 57.0° and 62.8°, corresponding to the (111), (220), (311), (400), (422), (511) and (440) reflections of magnetite (Fe_3O_4), respectively, which are in agreement with the standard pattern published for inverse cubic spinel Fe_3O_4 (COD 9002331) [22]. It is well known that the XRD patterns of both maghemite ($\gamma - Fe_2O_3$) and Fe_3O_4 [36] are similar, thus oxidation of the magnetite phase cannot be excluded. Indeed, the RIR refinement quantification analysis of the XRD patterns for the powdered iron oxide confirmed the presence of mainly Fe_3O_4 and a small amount of γ-Fe_2O_3.

The XRD patterns of the magnetic nanocomposites (GF@Fe_3O_4 and GF@CuS−Fe_3O_4) also exhibit the diffraction peaks of Fe_3O_4 (Fig. 1), hence indicating that the supported Fe_3O_4 preserved the inverse spinel crystalline structure. For both nanocomposites, the RIR refinement of their diffraction patterns confirms the successful incorporation of Fe_3O_4 on GF with γFe_2O_3:Fe_3O_4 − ratio (1:50) also observed for pristine Fe_3O_4 nanoparticles. Interestingly, there is a significant decrease in the intensity of the GF (002) diffraction peak in the XRD pattern of GF@CuS when compared to that of the parent GF (Fig. 1B), suggesting that face-to-face stacking of GF is absent. This diffraction line is shifted to lower 2θ angles and corresponds to slightly larger interlayer spacing than that of the pristine GF. Thus, it is suggested that the Fe_3O_4 nanoparticles act as spacers in keeping the suspended GF sheets/flakes separated [37]. Nevertheless, the observed shift is very small and the interlayer spacing values for GF@Fe_3O_4 and GF@CuS (3.41 Å) are very close to that of pristine GF (3.40 Å) and GF@CuS−Fe_3O_4 nanocomposites (3.36 Å). Although the XRD pattern of GF@CuS−Fe_3O_4 does not show any isolated diffraction peaks corresponding to the CuS phase, the RIR refinement analysis of the diffraction pattern confirms the presence of CuS (14.3%), magnetite (57.0%) and graphitic phase (28.4%), with traces of the oxidized phases $CuSO_4$ and maghemite (less than 3%), nevertheless confirming the successful incorporation of both CuS and Fe_3O_4 nanoparticles on GF. The average diameter (d_{XRD}) of the metal oxide/sulfide crystallites was estimated by using the Debye–Scherrer equation (eq. S8 in the Supplementary Material) [38] applied to the (311) and (110) reflections of Fe_3O_4 and CuS, respectively. These are the most intense reflections arising from the grafted NPs and do not overlap with any reflection from the GF substrate. According to these calculations, the average diameter of the incorporated NPs increases in the order of GF@CuS−Fe_3O_4 (5.3 nm Fe_3O_4) < GF@Fe_3O_4 (7.9 nm Fe_3O_4) *versus* 6.4 nm for the Fe_3O_4 particles. In the case of the GF@CuS composite, the average diameter of the grafted CuS nanoparticles is 11.9 nm *versus* 11.6 nm for the parent CuS particles.

The FTIR spectra of the GF−based nanocomposites as well as those of the pristine GF, CuS and Fe_3O_4 nanoparticles are shown in Fig. S2 in the Supplementary Material. The spectra of all GF−based materials present two bands at 2920 cm^{-1} and 2850 cm^{-1} assigned to C−H stretching modes that can be due to the existence of defects in the sp^2-hybridized

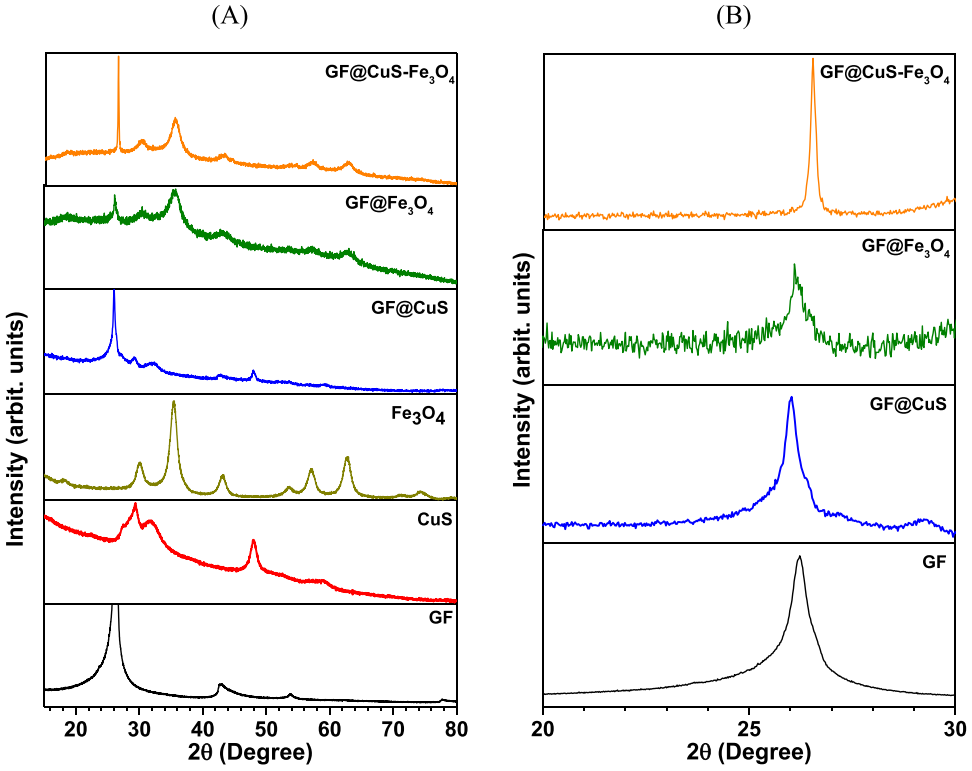

Fig. 1. (A) XRD patterns of pristine GF, CuS, Fe_3O_4 and the composite structures GF@CuS, GF@Fe_3O_4, and GF@CuS−Fe_3O_4; and (B) XRD patterns in the 2θ range of 20–30º, highlighting the shift of the graphite (002) reflection line upon nanoparticles incorporation.

domains of GF [39,40]. Furthermore, they present bands at 1630 cm^{-1} and 1577 cm^{-1} assigned to C=C stretching modes of GF skeletal vibrations from non−oxidized domains [41,42], an intense band at 1384 cm^{-1} that arises from the vibration modes of phenolic groups [43] and a broad band at 3440 cm^{-1} due to O−H stretching vibrations of the phenolic groups and adsorbed water [43,44]. The vibrational bands due to oxidised carbon species are observed at 1720 cm^{-1} (C=O), 1200 cm^{-1} (epoxy groups [39] and at 1120 cm^{-1} (overlapping of C−O−C and C−O stretching modes and C−O−H bending mode) [23,43, 45–47]. The FTIR spectrum of GF@CuS hybrid nanostructure shows the characteristic bands of GF and a band at 619 cm^{-1} characteristic of Cu–S stretching vibrations, confirming the incorporation of CuS [48] onto GF sheets (Fig. S2 in the Supplementary Material). The detailed discussion of FTIR spectrum of Fe_3O_4 NPs is presented in Suplementary Material).

The FTIR spectru of the GF@CuS−Fe_3O_4 nanocomposite show the characteristic bands of the three components, GF, Fe_3O_4 and CuS nanoparticles, which indicate the successful attachment of the nanoparticles onto GF. The comparison of FTIR spectra of GF@Fe_3O_4 and GF@CuS−Fe_3O_4 in the low energy region (800–450 cm^{-1}, Fig. S2 in the Supplementary Material) shows that the band associated with Fe−O stretching vibrations of pristine Fe_3O_4 (~560 cm^{-1}) is slightly shifted to higher wavenumber values in the spectra of the graphene−based counterparts (*i.e.*, GF@Fe_3O_4 and GF@CuS−Fe_3O_4). This has been reported as an indicator of the existence of interactions between the Fe_3O_4 nanoparticles and graphene for both nanocomposites (GF@Fe_3O_4 and GF@CuS−Fe_3O_4) [49,50]. In addition, the FTIR spectrum of GF@CuS−Fe_3O_4 shows a very weak band at 625 cm^{-1} that can be related to the presence of CuS. The band is shifted 6 cm^{-1} in comparison to the FTIR spectrum of pristine CuS and suggests some interaction between CuS and the other composite components. Moreover, the intensity of the band at 3420 cm^{-1} increases in comparison to pristine GF suggesting extensive surface hydroxylation of the composite nanoparticles.

A comparison between the Raman spectra (4000–150 cm^{-1}) of GF, pristine nanoparticles (Fe_3O_4 and CuS) and GF nanocomposites is established in Fig. 2. The Raman spectrum of the pristine GF shows two main bands at ~1356 cm^{-1} (D band) and ~1580 cm^{-1} (G band) with I_D/I_G= 0.4 (where I_D and I_D are the intensities of the D and G bands, respectivity), as well as three weak bands at ~2715 cm^{-1} (2D band), ~2947 cm^{-1} (D+G band) and ~3239 cm^{-1} (2D' band). In the case of the Raman spectra of GF decorated with metal oxide/sulfides materials, the 2D peak presents a shift of 11 cm^{-1} (GF@CuS), 14 cm^{-1} (GF@Fe_3O_4) and 23 cm^{-1} (GF@CuS−Fe_3O_4) when compared with that of the pristine GF, suggesting the decrease of electron concentration in the hybrids, *i.e.*, hole doping [51]. The location of the G band has been also used to reveal the interaction between the nanoparticles (CuS or/and Fe_3O_4) and the carbonaceous material [37]. For GF@Fe_3O_4 nanocomposite, the G band appears at 1587 cm^{-1} and is shifted to a higher wavenumber (8 cm^{-1}) relative to the Raman spectrum of the pristine GF. This shift is associated with the charge transfer between Fe_3O_4 NPs and graphene sheets and indicates the existence of interactions between the anchored particles and graphene [21,37]. For the D band almost no shift is observed in the Raman spectra of GF decorated with CuS or/and Fe_3O_4, with the maximum shift of 6 cm^{-1} being observed for GF@CuS.

The Raman spectrum of the GF@CuS nanocomposite, besides presenting the bands characteristic of GF, shows a band at 467 cm^{-1}, which is unambiguously attributed to S–S stretching vibration (473 cm^{-1}) [52, 53] and SO_4^{2-} symmetric bending vibration (460 cm^{-1}) modes [54], respectively. The Raman spectra of the Fe_3O_4 NPs as well as of the GF@Fe_3O_4 and GF@CuS–Fe_3O_4 samples show weak bands in the 800–150 cm^{-1} region, which were resolved into Gaussian−Lorentzian components (Fig. S3 and Table S1 in the Supplementary Material). The spectra of the Fe_3O_4 NPs, GF@Fe_3O_4 and GF@CuS–Fe_3O_4 exhibit the characteristic Raman phonon modes of the iron oxide component: A_{1g} (672 cm^{-1}), 3 T_{2g} (496, 453 and 175 cm^{-1}) and E_g (271 cm^{-1}) confirming that the iron oxide is mainly composed of magnetite (Fe_3O_4) [22, 55]. In addition to these bands, the phonon modes T_{2g} (358 cm^{-1}) and A_{1g} (724 cm^{-1}) can be assigned to maghemite ($\gamma - Fe_2O_3$), indicating the partial oxidation of the surface of the pristine Fe_3O_4 nanoparticles [56–59].

In the Raman spectra of GF@Fe_3O_4 and GF@CuS–Fe_3O_4 two additional bands are observed in the 215–222 cm^{-1} and 590–620 cm^{-1} regions (Table S1 in the Supplementary Information), which are attributed to Fe_3O_4 grown over the surface of GF or GF@CuS and are indicative of partial oxidation of magnetite to maghemite [60]. The position of the latter band suggests the existence of some interactions between the iron oxide nanoparticles and carbon [61], as was previously suggested by FTIR.

A detailed XPS analysis was performed in order to gain deeper insights into the surface chemistry of the hybrid materials described above. For the pristine GF material only signals corresponding to the presence of carbon (96.0 at%) and oxygen (4.0 at%) are detected (Table S2 in the Supplementary Material). The C 1 s high−resolution spectrum of GF was deconvoluted into six peaks (Table S3 in the Supplementary Material): the main band at 284.6 eV related to the graphitic structure (sp^2), a band at 286.2 eV assigned to sp^3 C–C in aromatic rings, a band at 287.0 eV attributed to C−OH in alcohols and phenols, a band at 288.0 eV associated with C−O−C bonds, a band at 288.9 eV

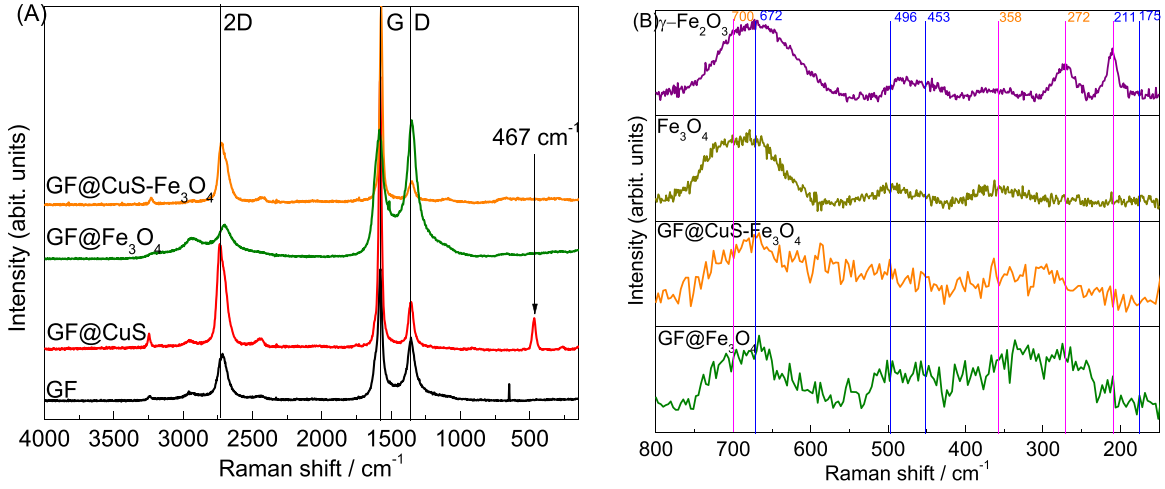

Fig. 2. Raman spectra of pristine GF and its composites, Fe_3O_4 and $\gamma - Fe_2O_3$: (A) whole region and (B) low Raman shift region (800–150 cm^{-1}). The blue lines are related to magnetite bands and the pink lines are associated with the maghemite component.

attributed to O–C═O bonds in carboxylic acids, carboxylic anhydrides and esters, and the $\pi - \pi^*$ shake−up satellite band from the sp^2 −hybridized carbon atoms at 290.8 eV [62,63] (Fig. S4 in the Supplementary Material). The O 1 s spectrum of the pristine GF was deconvoluted into three components (Fig. S4 and Table S3 in the Supplementary Material) at 531.2 eV associated with O═C in carbonyl or quinone groups, at 532.6 eV from O–C in phenol or/and epoxy groups and a component at 533.7 eV related to –O– in carbonyl groups [64] and/or adsorbed water and oxygen. Representative XPS spectra of the Cu 2p and S 2p core–level regions for the hybrid GF@CuS are shown in Fig. 3. The Cu 2p high-resolution XPS spectrum of GF@CuS nanocomposite shows a doublet at 932.2 eV (Cu $2p_{3/2}$) and 952.0 eV (Cu $2p_{1/2}$), which is in agreement with the published values for CuS. An additional doublet is located at 934.9 (Cu $2p_{3/2}$) and 954.3 eV (Cu $2p_{1/2}$) corresponding to a Cu–O linkage [65], which has been confirmed by the peak at 530.6 eV in the O 1 s XPS spectrum (Table S3 in the Supplementary Material). The presence of this doublet suggests that the interaction between the CuS phase and the GF occurs through Cu–O bonds. Besides both doublets, shake-up satellite peaks are observed in the Cu $2p_{3/2}$ region at approximately 940.4 eV and 944.1 eV, which are indicative of the presence of paramagnetic Cu^{2+} chemical state [66,67]. On the other hand, the S 2p high-resolution XPS spectrum indicates that there are distinct sulfur species in the nanocomposite. The peak at 162.3 eV corresponds to CuS and is also in agreement with reported values [65,67]. The other peak at 168.5 eV is attributed to oxidized sulfur from sulfate groups, indicating that oxidation occurred to a slight extent [67].

The XPS spectrum of the pristine Fe_3O_4 NPs confirms that the material is mainly composed of Fe (30.8%) and O (51.5%) and is discussed in detail in the Supplementary Material. The deconvolution of the Fe 2p high-resolution spectrum of that nanomaterial is shown in Fig. 4, and the analysis suggests the partial oxidation of Fe_3O_4 to γ-Fe_2O_3. The XPS characterization of the GF@Fe_3O_4 nanocomposite confirms the presence of the expected elements (Table S2 in the Supplementary Material). Similarly to the pristine GF, the C 1 s high−resolution spectrum of GF@Fe_3O_4 was resolved into six component bands related to sp^2 and sp^3 carbon and oxidised carbon species. The binding energies (BEs) of the bands related to sp^2 and sp^3 carbon are the same for both GF and GF@Fe_3O_4 materials, whereas the bands corresponding to oxidised carbon species are shifted to higher BEs. In particular, a shift of 0.3 eV was observed for the band related to C−O and suggests some interaction/bond formation between C−O and Fe. The possible formation of the Fe–C bond can be excluded from the C 1 s spectrum of GF@Fe_3O_4 since C–Fe bonds should be present at ~283.3 eV [37]. Moreover, no band at 707.5 eV attributed to Fe–C bond [37,68] is detected in the Fe 2p high-resolution spectrum of that sample, which confirms the lack of Fe–C bonds.

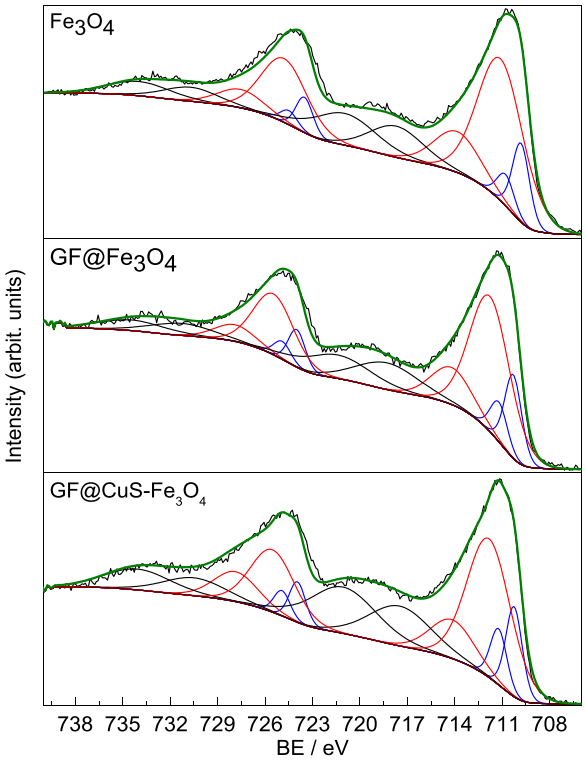

Fig. 4. Fe 2p high-resolution XPS spectra of pristine Fe_3O_4 and composites.

The Fe 2p high-resolution spectrum of GF@Fe_3O_4 was resolved into two doublets (Fe $2p_{3/2}$ and Fe $2p_{1/2}$) and two satellite bands in the $2p_{3/2}$ and $2p_{1/2}$ regions (Fig. 4B and Table S3 in the Supplementary Material). All the bands of the Fe 2p region for GF@Fe_3O_4 are slightly shifted to higher BEs relative to those in the Fe 2p spectrum of the pristine Fe_3O_4 NPs, which can be due to the oxidation of Fe_3O_4 [69] or/and bonding to GF. As was observed for the pristine Fe_3O_4, the determined Fe^{2+}/Fe^{3+} ratio is 0.4 for GF@Fe_3O_4, suggesting the presence of Fe_3O_4 and a small amount of $\gamma - Fe_2O_3$ on the composite surface. The O 1 s spectrum of GF@Fe_3O_4 includes a band assigned to O−Fe (530.3 eV) and three components (>531 eV) due to oxidized carbon species. The ratio of the area of these bands (C−OH, C−O−C and O−C═O) found in the C 1 s region and their counterparts in the O 1 s region is close to 0.9. The Fe/(O–Fe) ratio, is 0.76, being close to the expected value of 0.75, which confirms that the graphene flakes were successfully decorated with iron oxide nanoparticles.

The XPS analysis of GF@CuS–Fe_3O_4 tricomponent nanocomposite

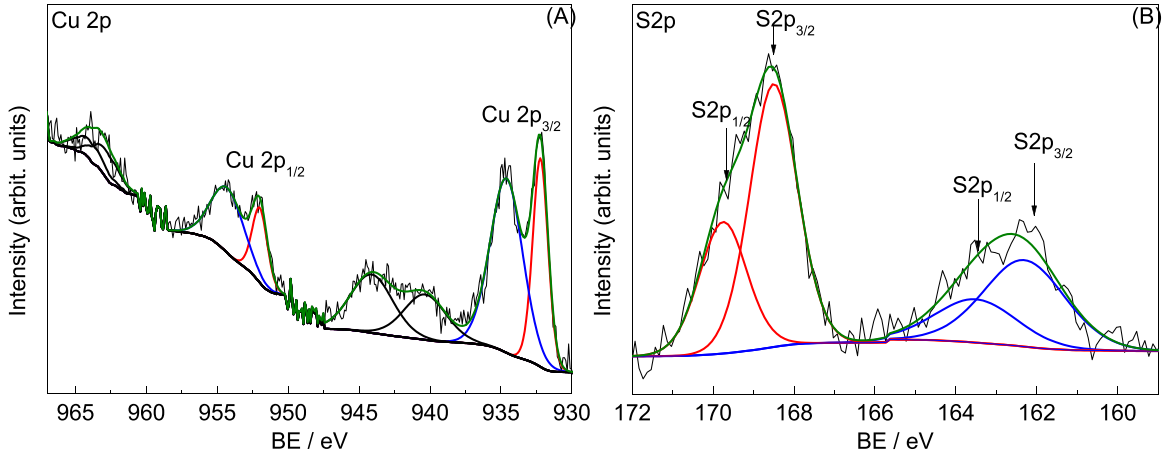

Fig. 3. High-resolution XPS spectra of GF@CuS in (A) Cu 2p and (B) S 2p core-level regions.

shows that its surface composition consists of carbon (50.1 at%), oxygen (30.3 at%), iron (17.8 at%), copper (0.3 at%) and sulfur (0.5 at%), Table S2 in the Supplementary Material. From the deconvolution of the C 1 s high-resolution spectrum of GF@CuS−Fe_3O_4, it was found that the C−O band suffers a shift of 0.6 eV in comparison with the BE of that band in the C 1 s spectrum of the pristine GF (Table S3 in the Supplementary Material), suggesting some interaction between C−O and both CuS and Fe_3O_4 nanoparticles. The deconvolution of the Fe 2p high-resolution spectrum of GF@CuS–Fe_3O_4 (Fig. 5C) reveals that the values of $Fe^{2+}/Fe^{3+}$and Fe/O ratios (0.4 and 1.0, respectively) are similar to those found for GF@Fe_3O_4, which suggests that Fe_3O_4 and $\gamma - Fe_2O_3$ species are present on the surface of the GF@CuS–Fe_3O_4 composite surface. Furthermore, the analysis of the S 2p spectrum of GF@CuS−Fe_3O_4 confirms the presence of S^{2-} and SO_4^{2-} states, suggesting some CuS oxidation to $CuSO_4$.

Fig. 5 shows representative SEM images of the Fe_3O_4 and/or CuS nanoparticles supported on the GF nanosheets (GF@CuS, GF@Fe_3O_4 and GF@CuS−Fe_3O_4). The composition of the nanocomposites was confirmed by EDS, indicating that they are mainly composed of C (91.2 at%), O (6.6 at%), S (0.9 at%) and Cu (0.9 at%) for GF@CuS (Fig. S5A in the Supplementary Material) and C (78.5 at%), O (10.5 at%) and Fe (11.1 at%) for GF@Fe_3O_4 (Fig. S5B in the Supplementary Material). GF@CuS−Fe_3O_4 contains C (88.3 at%), O (10.8 at%) and Fe (0.9 at%). The absence of Cu and S signals in the EDS spectrum of GF@CuS−Fe_3O_4 (Fig. S5C in the Supplementary Material) can be ascribed to their content being under the detection limit of the technique.

3.2. RhB adsorption properties

In order to evaluate the application of pristine GF and their nanocomposites as photocatalysts, the adsorption behavior and photocatalytic performance of the materials were studied by using RhB as a model organic dye.

The effect of the contact time on the RhB adsorption capacity of GF, GF@CuS, GF@Fe_3O_4 and GF@CuS−Fe_3O_4 is shown in Fig. S6 in the Supplementary Material. In general, the RhB adsorption was faster at the initial stages of the contact period, and thereafter it became slower near the equilibrium. This observation agrees with the existence of a larger number of vacant surface sites for adsorption during the initial stage as compared with after a lapse of time; the remaining vacant surface sites are less occupied due to repulsive forces between the solute molecules on the solid and bulk phases [70]. The removal of the dye from solution reaches its maximum value after 30 min for GF, while for GF@Fe_3O_4 and GF@CuS materials, the dye removal needs more time to reach equilibrium (120 min and more than 180 min, respectively), Fig. S6 in the Supplementary Material. For the GF@CuS−Fe_3O_4, the adsorption capacity (q_e^{exp}) is 2.1 mg g^{-1}, which is considerably lower than that of pristine GF and GF@CuS and GF@Fe_3O_4 nanocomposites (Table 1). The adsorption capacity changes in the following order: GF (62.3 mg g^{-1}) > GF@CuS (56.5 mg g^{-1}) > GF@Fe_3O_4 (20.0 mg g^{-1}) >> GF@CuS--Fe_3O_4 (2.1 mg g^{-1}). This suggests that the GF@CuS−Fe_3O_4 composite almost does not adsorb RhB, presenting a sorption efficiency of 6.5% after 180 min of contact period. For this reason, the sorption kinetic was not further studied for this nanocomposite. For the other materials, the sorption efficiency after 180 min of contact period is significantly higher and decreases in the order of: GF (97.6%) < GF@CuS (60.9%) < GF@Fe_3O_4 (31.9%).

3.2.1. Adsorption kinetics

The sorption process commonly takes place in three steps: (a)

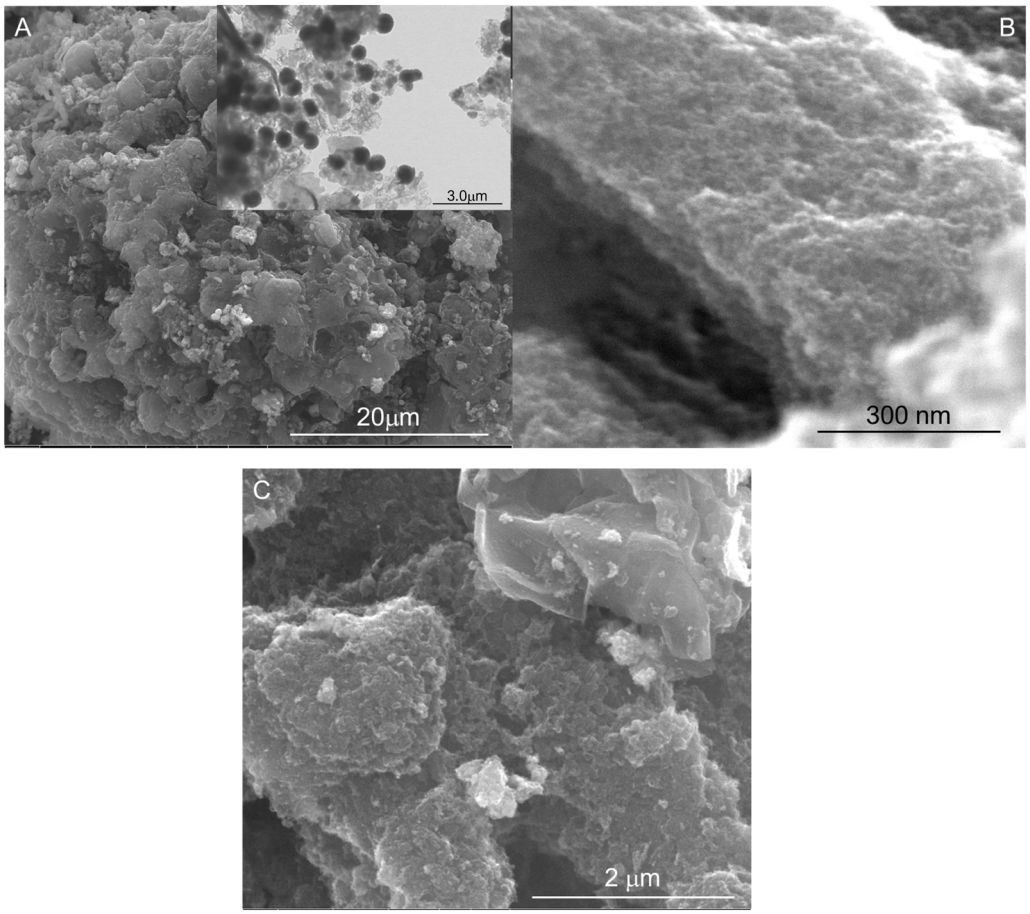

Fig. 5. SEM images of (A) GF@CuS (inset: STEM image), (B) GF@Fe_3O_4, and (C) GF@CuS−Fe_3O_4 hybrid nanostructures.

Table 1
Adsorption kinetic parameters of RhB onto adsorbents[a].

Model	Material	Parameters								
Pseudo−first order		q_e^{exp} (mg g^{-1})	q_e^{calc} (mg g^{-1})	k_1 (min^{-1})	R^2					
	GF	62.3	39.8	9.30×10^{-2}	0.96					
	GF@CuS	56.5	46.7	2.30×10^{-2}	0.85					
	GF@Fe_3O_4	20.0	14.7	2.10×10^{-2}	0.96					
Pseudo−second order		q_e^{exp} (mg g^{-1})		q_e^{calc} (mg g^{-1})		h (mg g^{-1} min^{-1})		k_2 (g mg^{-1} min^{-1})		R^2
	GF	62.3		63.7		23.87		5.88×10^{-3}		0.99
	GF@CuS	56.5		58.5		6.12		2.00×10^{-3}		0.97
	GF@Fe_3O_4	20.0		20.6		1.62		3.80×10^{-3}		0.97
Elovich				a_e (mg g^{-1} min^{-1})		b_e (g mg^{-1})		R^2		
	GF			38.65		0.07		0.99		
	GF@CuS			31.23		0.12		0.98		
	GF@Fe_3O_4			11.45		0.37		0.99		
Intra-particle diffusion		k_{id}^1	C_1	R^2	k_{id}^2	C_2	R^2	k_{id}^3	C_3	R^2
	GF	17.66	1.79	0.95	9.56	17.00	0.97	0.42	57.47	0.64
	GF@CuS	10.08	1.62	0.92	4.79	12.06	0.99	1.58	35.86	0.96
	GF@Fe_3O_4	4.19	0.33	0.99	1.15	5.29	0.98			
Bangham		k_b (mg g^{-1} min^{-1})		a		R^2				
	GF	4.44×10^{-1}		0.28		0.94				
	GF@CuS	3.66×10^{-1}		0.18		0.98				
	GF@Fe_3O_4	3.12×10^{-1}		0.13		0.98				
Boyd		R^2								
	GF	0.99								
	GF@CuS	1.00								
	GF@Fe_3O_4	0.96								

[a)] q_e^{exp} and q_e^{calc} are the experimental and calculated amounts of RhB adsorbed (mg g^{-1}) at the equilibrium time, respectively; k_1 is the pseudo-first-order rate constant of RhB sorption (min^{-1}); h is the pseudo−second order initial adsorption rate (mg $g^{-1}min^{-1}$); k_2 is the pseudo−second order adsorption rate (mg $g^{-1}min^{-1}$); a is the initial sorption rate constant (mg g^{-1} min^{-1}); b_e is related to the extent of surface coverage and the activation energy for chemisorption (g mg^{-1}); k_{id}^{1-3} is the intra−particle diffusion rate constant of 1st, 2nd and 3rd stage, respectively (mg g^{-1} $min^{-0.5}$); R^2 is the correlation coefficient.

transfer of the solute species from the bulk solution into the external surface of the sorbent; (b) surface diffusion or pore diffusion process, whereby the solute molecules diffuse to sorption sites; (c) chemical or physical sorption, in which the sorption happens at an external or internal site of the sorbent surface. Either one or a combination of these steps determines the rate of sorption [27]. In order to determine which mechanism is the rate−determining step, the kinetic studies were done using six kinetic models including Lagergren first−order [25], the McKay and Ho pseudo−second order [26], Weber−Morris intraparticle diffusion [27], Elovich [28,29], Bangham [30,31] and Boyd [32,33] models.

In the pseudo−second−order kinetic model, the rate−controlling step of adsorption is the interaction between the adsorbent and adsorbate, such as ion sharing and transferring. The Elovich model describes ion exchange in a liquid phase. The Weber−Morris intra−particle diffusion and Bangham models assume that internal diffusion and channel diffusion are the determining steps to control the adsorption rate, respectively [71]. The Boyd model assumes that the main resistance to diffusion is the boundary layer surrounding the adsorbent particle [72].

The fitting results obtained from different models are summarised in Table 1. When the pseudo−second order kinetic model was applied, the experimental q_e^{exp} values agree well with the calculated ones (q_e^{cal}), obtained from the linear plot. The correlation coefficients for this model are high and change from 0.97 for GF@CuS and GF@Fe_3O_4 to 0.99 for GF. Although the correlation coefficients for the pseudo−first−order kinetic model are also relatively high and change from 0.85 for GF@CuS to 0.96 for GF@Fe_3O_4 and GF, the calculated q_e^{cal} values do not agree with the experimental q_e^{exp} values. Therefore, the adsorption of RhB on all studied adsorbents could be well described by the pseudo−second−order kinetic model (Fig. 6). This indicates that the pseudo−second−order adsorption mechanism is predominant and the overall rate of the RhB adsorption process is controlled and limited by chemisorption. Elovich equation is also successfully used to describe second-order kinetics assuming that the actual solid surfaces are energetically heterogeneous, but the equation does not propose any definite mechanism for adsorbate–adsorbent. Anyway, the studied systems also

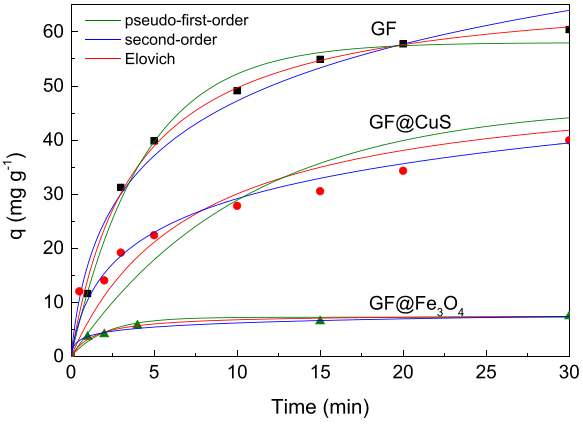

Fig. 6. Adsorption profiles of RhB onto GF, GF@CuS and GF@Fe_3O_4 and fitting of the experimental data using pseudo-first order, second-order and Elovich models.

follow the Elovich model (Fig. 6) with high correlation coefficients ($R^2 \geq 0.98$). The fitting of the experimental results of RhB adsorption on the different materials using the different models, which are presented in Fig. 6, indicates that the Elovich model best describes the RhB adsorption onto pristine GF, while in the case of the GF@CuS and GF@Fe_3O_4 nanocomposites both the pseudo−second−order and Elovich models are applicable to describe the RhB adsorption process and the chemical interaction between RhB and the adsorbent may be involved in adsorption. Similar behaviour was observed for tannic acid functionalized graphene [73] and reduced graphene oxide (rGO) and its composites [74].

3.2.2. *Adsorption mechanism*

The abovementioned pseudo−first−order and pseudo−second−−order kinetic models are not able to identify the diffusion mechanism of the adsorption of RhB on pristine GF and their composites. Therefore,

the kinetic data were subjected to analysis by the intra−particle diffusion model for the diffusion mechanism. The segmental linear regression analysis of the data shows that the q *vs.* $t^{0.5}$ curves have three different regions (Fig. S7 in the Supplementary Material). The first region is the instantaneous adsorption, representing the mass transfer of adsorbate molecules from the bulk solution to the adsorbent surface. The second region is the gradual adsorption stage, where intraparticle diffusion is the rate−limiting step. The third region is the final equilibrium stage, where intraparticle diffusion started to slow down due to the extremely low adsorbate concentrations left in the solution and represents the adsorption−desorption equilibrium section [75]. The linear plots of the second and third stages did not pass through the origin. This implied that, during the adsorption process, film diffusion and intraparticle diffusion exist simultaneously, and intraparticle diffusion is not the only rate−limiting step in the overall adsorption process [76]. To distinguish between the pore and film diffusion steps involved in the adsorption process, the kinetic results were further analysed using the Boyd model. According to that model, the three sequential steps in the adsorption are: (i) film diffusion, in which the dye travels towards the external surface of the adsorbent; (ii) particle diffusion, in which the dye diffuses within the pores of the adsorbent; and (iii) adsorption of the dye into the interior surface of the adsorbent. If the B_t (Boyd parameter) *versus* time plot passes through the origin, pore diffusion is the rate−limiting step. If the plot does not pass through the origin, the adsorption process is film diffusion controlled or chemical reaction dominates the adsorption rate [72]. As illustrated in Fig. S8 in the Supplementary Material, the linear curves do not pass through the origin, indicating that the adsorption of RhB onto GF and their nanocomposites is mainly governed by a film diffusion-controlled mechanism [75].

3.2.3. Photocatalytic tests

The photocatalytic activity of the hybrid nanostructures as well as of the neat components on the photodegradation of RhB dye, under visible light irradiation, was evaluated using UV-Vis spectroscopy. Before light exposure, the solution containing the RhB dye and the photocatalysts was stirred in the dark. Small values of RhB degradation under visible-light irradiation were observed in the absence of catalyst (10% after 60 min). However, upon the addition of a small amount of H_2O_2 (0.1 wt %), about 28% of RhB was degraded after 60 min, which could be attributed to the photolysis of H_2O_2 to form reactive·OH (H_2O_2 +visible light →·OH+OH^-) [77]. Whereas in the presence of H_2O_2 but in the darkness conditions, no degradation of RhB was observed, for the same reaction time (Fig. 7). The experiments using GF as catalyst (under light irradiation in the presence and in the absence of H_2O_2) give very similar results suggesting that adsorption is the dominat process (Fig. S9 in the Supplementary Material). The adsorption process was dominat also wthen GF@CuS, GF@Fe_3O_4 and GF@CuS−Fe_3O_4 were tested in RhB photodegradation without H_2O_2 addition.

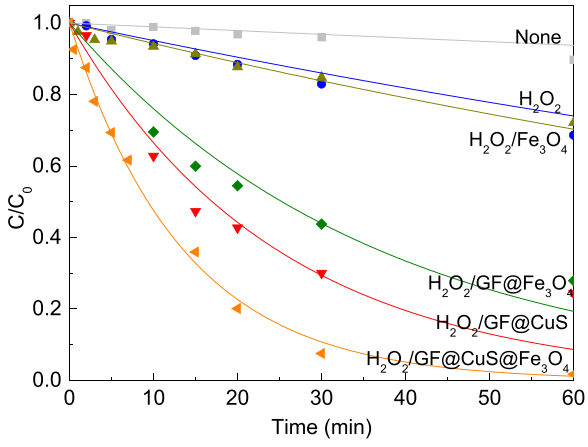

Fig. 7. Photocatalytic degradation profiles of RhB over different catalysts and corresponding fits using the pseudo-first order model.

When the photocatalytic reactions were performed in the presence of the Fe_3O_4 NPs, and H_2O_2, 31% of RhB was degraded, which is attributed to the activation of H_2O_2 to form reactive •OH by nanoparticles and reactive charge carriers produced from Fe−O [77] (Fig. 7). In fact, in the presence of binary/ternary graphene nanocomposites, the RhB degradation efficiencies were much higher than those obtained with the pristine nanomaterials (CuS or Fe_3O_4). The RhB degradation values for GF@CuS, GF@Fe_3O_4 and GF@CuS−Fe_3O_4 after 60 min light irradiation were 76%, 81% and 98%, respectively (Fig. 7). Encouragingly, the experimental results demonstrate that graphene nanocomposites have better photocatalytic efficiency than the pristine nanoparticles in the whole photocatalytic process, and that GF@CuS−Fe_3O_4 presents the best photocatalytic activity. The variation of the UV−Vis absorption spectra of RhB degradation over time is shown in Figs. S10–S12 in the Supplementary Material, in the presence of GF@CuS−Fe_3O_4, GF@ −Fe_3O_4 and GF@CuS nanocomposites.

The kinetic behaviour of photocatalytic degradation of RhB was studied. It is assumed that in all cases, the photocatalytic process follows the first−order kinetic rate equation:

$$\ln(C/C_0) = -kt$$

where C_0 and C (mg L^{-1}) are the concentrations of RhB at $t = 0$ and time t (min), respectively, and k (min^{-1}) is the rate constant.

The data fitting of RhB photocatalytic degradation in the absence of the photocatalysts (*i.e.*, under light irradiation and in the presence of H_2O_2) and in the presence of Fe_3O_4 NPs, GF@CuS, GF@Fe_3O_4 and GF@CuS−Fe_3O_4 hybrid nanocomposites is shown in Fig. 7 and the results of the fitted parameters are summarized in Table S4 in the Supplementary Material. The pseudo−first-order rate constant (k) of RhB removal over GF@CuS−Fe_3O_4 is 2.1, 5.1 and 15.0 times higher than those of GF@CuS, GF@Fe_3O_4 and pristine Fe_3O_4, respectively. Compared with literature data, the k values for the collective removal (adsorption and photocatalysis) of RhB over Fe_2O_3–TiO_2 graphene aerogel nanocomposites changed in the range of (33.86–59.44)× 10^{-3} min^{-1} and depended on the component ratio in the composite [78]. These values are lower than that found in this work for the ternary nanocomposite ($k = 70.5 \times 10^{-3}$ min^{-1}). For ultrathin graphene oxide encapsulated in a uniform metal organic framework [77] (MIL−88 A (Fe)), the pseudo−first-order rate constant for photodegradation of RhB ($k = 64.5 \times 10^{-3}$ min^{-1}) is slightly lower than obtained in this work. Besides that, the materials prepared and studied in this work are even more satisfactory considering the operating parameters (lamp power (500 W [77,78] *versus* 150 W in this work), operating time (80 min [77] *versus* 60 min in this work), the dosage of adsorbents/photocatalysts (0.4 g $L^{1\ 88}$ *versus* 0.2 g L^{-1} in this work) and the treated volume of RhB solution (50 mL [77] or 25 mL [78] *versus* 100 mL in this work). This confirms the superiority of the resulting materials in the elimination of organic dyes in wastewater.

To identify the species produced in the photodegradation of RhB, the temporal proton NMR profiles of the dye, and final products were monitored in DMSO−d_6. The ^{1}H NMR spectrum of RhB (Fig. 8) shows the typical proton NMR signals of pure rhodamine: the NMR signals of the aromatic hydrogens (H_d, H_e, H_f, and H_g) were located at $\sigma = 6.80$–8.30 ppm, (Fig. 8), while those of H_a and H_b of the N − diethyl group appeared at $\sigma = 1.14$–1.24 ppm and 3.67–3.53 ppm, respectively.

During the photocatalytic degradation of RhB in the presence of GF@Fe_3O_4 and GF@CuS−Fe_3O_4 photocatalysts, a series of new signals appeared at 1.10–1.30 ppm (hydrogen from CH_3 and analogous groups), 1.81, 2.00–2.93, and 8.30–8.50 ppm. When the reaction occurs in the presence of GF@CuS, additional bands appear at 7.07–7.33 ppm (aromatic protons). This could be associated with either the deethylation process or the breakdown of the xanthene ring [79]. For all photocatalysts, the characteristic signals of RhB assigned to aliphatic and

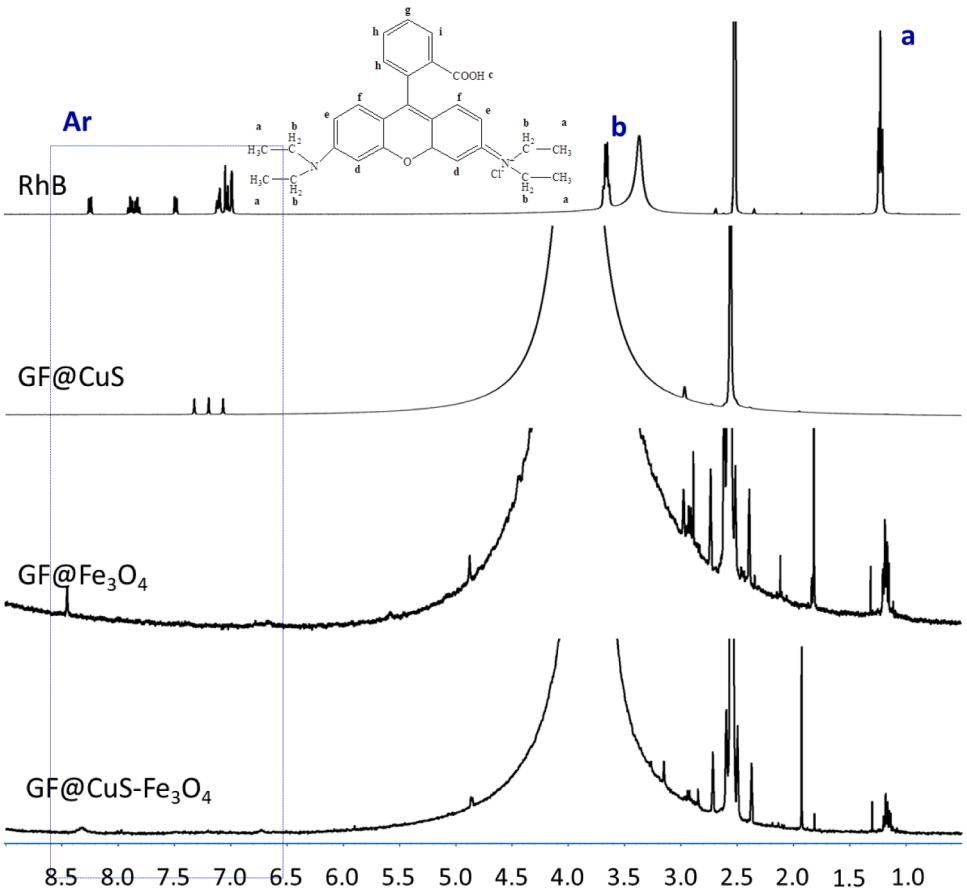

Fig. 8. ^{1}H NMR spectra of RhB before and after the photocatalytic degradation in the absence and in the presence of composite photocatalysts under visible light irradiation. Initial concentration of RhB: 1.3×10^{-5} M.

aromatic protons almost disappeared. These results indicate that the destruction of the conjugated structure of RhB occurred in the suspension during irradiation. Anyway, when the GF@CuS and GF@CuS−Fe_3O_4 composites were applied as photocatalysts, less breakdown of RhB products is formed. Thus, the GF@CuS−Fe_3O_4 composite is the best photocatalyst, not only due to the shortest degradation time, but also due to the number of secondary products formed.

To assess the reusability of the best performance catalyst in the photocatalytic degradation of RhB, three consecutive catalytic cycles were performed under identical experimental conditions (Fig. S13 in the Supplementary Material). The GC@CuS−Fe_3O_4 catalyst can be efficiently reused for at least three cycles, achieving total removal of RhB. Nevertheless, the reaction time increases from 60 min in the 1st cycle to 150 min in the 3rd cycle. AAS was performed to assess the eventual metals leaching from the catalyst to the reaction medium. No leaching of Cu and Fe was observed, as their concentrations in solution after the catalytic cycles were under the detection limit of the equipment.

Thus, the increase of time required for the total degradation of RhB in consecutive cycles may be due to changes in the catalyst structure/composition or adsorption of RhB partial-photodegradation products on the materials surface, blocking the accessibility of the substrate to the active sites during the re-use cycles. In order to unveil the reasons for such increase of reaction time, the zeta potential of GC@CuS−Fe_3O_4 aqueous dispersion was measured before and after the catalytic tests. The zeta potential of the as-prepared GC@CuS−Fe_3O_4 is 20.3 mV, indicating that the surface of the material is slightly positively charged. After the 3rd catalytic cycle, the zeta potential of the material decreases to 0.5 mV, which suggests the existence of particle aggregation, and may be the cause of the increase of the reaction time by decreasing the available surface area for the photocatalytic reaction to occur.

The XRD partterns of both the as-prepared GF@CuS−Fe_3O_4 catalyst and after the last catalytic cycle are similar, suggesting that no major structural changes occurred during the catalytic process. However, the M(*H*) curves of the parent and recycled GF@CuS−Fe_3O_4 catalyst (after three catalytic cycles) at 300 K, obtained by SQUID magnetometry and presented in Fig. S14 in the Supplementary Material, reveal a decrease of the saturation magnetization at that temperature from 36.7 to 23.6 emu g^{-1}. Such saturation magnetization suppression may be explained by the partial oxidation of Fe_3O_4 to γ-Fe_2O_3, which has lower M_S value than Fe_3O_4.[91] A similar suppression is also observed for the GF@CuS−Fe_3O_4 sample after 2 years of storage without any special care, where slow oxidation of Fe_3O_4 to γ-Fe_2O_3 by contact with the oxygen from the air was observed.

4. Conclusions

We have demonstrated a facile wet chemical route to synthesize nanocomposites of graphene flakes with CuS, Fe_3O_4 and CuS−Fe_3O_4. The preparation method is easily scalable and follows green strategies, without using any graphene oxidation/reduction process. A series of characterisation methods have demonstrated successful attachment of copper sulfide and iron oxide nanoparticles onto the graphene flakes.

Visible−light−induced degradation of RhB over the nanosized GF−based composites was observed. The GF@CuS−Fe_3O_4 composite exhibited high activity for the RhB degradation (up to 98% after 60 min reaction time). The development of GF nanocomposite photocatalytic technologies requires a deeper understanding of their characteristics. The detailed kinetics and mechanisms in this work should provide valuable knowledge in this respect. This system possesses several advantages: (i) the strong photooxidative ability to degrade dye pollutants,

(ii) the mild reaction conditions, including the pH values.

All of these suggest that the idea of using GF nanocomposites could be a plausible strategy to develop an efficient visible−light−driven photocatalyst for wastewater dye pollutants removal.

Funding

Support for this work was provided by Fundação para a Ciência e a Tecnologia (FCT)/ MCTES in the framework of the projects UIDB/50006/2020 and UIDP/50006/2020 (LAQV-REQUIMTE) and projects UIDB/50011/2020, UIDP/50011/2020 and LA/P/0006/2020 (CICECO-Aveiro Institute of Materials). The work was also supported by the UT Austin|Portugal Program through project UTAP−ICDT/CTM−NAN/0025/2014.

CRediT authorship contribution statement

Iwona Kuźniarska-Biernacka: Conceptualization, Formal analysis, Investigation, Methodology, Supervision, Validation, Writing – original draft, Writing – review & editing. **Cristina Freire:** Conceptualization, Validation. **Mariana Rocha:** Formal analysis, Investigation, Methodology, Writing – review & editing. **João H. Belo:** Formal analysis, Investigation, Writing – original draft. **João Pedro Araújo:** Formal analysis, Writing – original draft. **Ana C. Estrada:** Formal analysis, Investigation, Methodology, Validation, Writing – original draft, Writing – review & editing. **Clara Pereira:** Formal analysis, Methodology, Supervision, Validation, Writing – original draft, Writing – review & editing. **Tito Trindade:** Conceptualization, Formal analysis, Funding acquisition, Methodology, Supervision, Validation, Writing – review & editing. **Cristina Freire:** Formal analysis, Funding acquisition, Conceptualization, Methodology, Supervision, Writing – review & editing. **Brian A. Korgel:** Funding acquisition, Methodology, Validation, Writing – review & editing. **Renata Matos:** Investigation. **Joana L. Lopes:** Investigation. **Tushti Shah:** Investigation, Methodology, Writing – review & editing. All authors have read and agreed to the published version of the manuscript.

Declaration of Competing Interest

The authors declare that they have no known competing financial interests or personal relationships that could have appeared to influence the work reported in this paper.

Data Availability

Data will be made available on request.

Acknowledgements

M. Rocha thanks the junior researcher contract funded by European Union's Horizon 2020 Research and Innovation Programme under Grant Agreement No. 863307 (H2020-FETOPEN-2018-2019-2020-01). C. Pereira thanks FCT for funding through the Individual Call to Scientific Employment Stimulus (Ref. 2021.04120. CEECIND/CP1662/CT0008). The research effort of T. Shah and B.A. Korgel was also partially supported by the Robert A. Welch Foundation (grant no. F-1464) and the National Science Foundation through the Center for Dynamics and Control of Materials: an NSF MRSEC under Cooperative Agreement No. DMR-1720595. J. H. Belo thanks EEA grants *via* the project FBR OC1 85, PARSUK-FCT *via* project SMARTX and FCT for the projects PTDC/EME-TED/3099/2020 and CERN/FISTEC/0003/2019 and for his contract DL57/2016 reference SFRH-BPD-87430/2012. I. Kuźniarska-Biernacka thanks FCT for funding through program DL 57/2016–Norma transitória REQUIMTE/EEC2018/14. Joana L. Lopes thanks FCT for doctoral grant (SFRH/BD/126241/2016). Ana C. Estrada also acknowledges the costs of her research contract resulting from the FCT hiring funded by National funds (OE), through FCT, I.P., in the scope of the framework contract foreseen in 4, 5, and 6 of article 23 of the Decree-Law 57/2016, of 29 August, changed by the law 57/2017, of 19 July.

Appendix A. Supporting information

Supplementary data associated with this article can be found in the online version at doi:10.1016/j.cattod.2023.114132.

References

[1] C. Belver, J. Bedia, A. Gómez-Avilés, M. Peñas-Garzón, J.J. Rodriguez, Chapter 22 - semiconductor photocatalysis for water purification, in: S. Thomas, D. Pasquini, S.-Y. Leu, D.A. Gopakumar (Eds.), Nanoscale Materials in Water Purification, Elsevier, 2019, pp. 581–651.
[2] E. Mendoza-Mendoza, A.G. Nuñez-Briones, R. Leyva-Ramos, R.D. Peralta-Rodríguez, L.A. García-Cerda, E.D. Barriga-Castro, R. Ocampo-Pérez, J. Rodríguez-Hernández, A novel two-step route for synthesizing pure Ta2O5 nanoparticles with enhanced photocatalytic activity, Ceram. Int. 45 (2019) 6268–6274.
[3] J. Shen, G. Ma, J. Zhang, W. Quan, L. Li, Facile fabrication of magnetic reduced graphene oxide-ZnFe2O4 composites with enhanced adsorption and photocatalytic activity, Appl. Surf. Sci. 359 (2015) 455–468.
[4] U.T.D. Thuy, N.Q. Liem, C.M.A. Parlett, G.M. Lalev, K. Wilson, Synthesis of CuS and CuS/ZnS core/shell nanocrystals for photocatalytic degradation of dyes under visible light, Catal. Commun. 44 (2014) 62–67.
[5] M. Saranya, C. Santhosh, R. Ramachandran, P. Kollu, P. Saravanan, M. Vinoba, S. K. Jeong, A.N. Grace, Hydrothermal growth of CuS nanostructures and its photocatalytic properties, Powder Technol. 252 (2014) 25–32.
[6] S.A. Kulkarni, P.S. Sawadh, P.K. Palei, K.K. Kokate, Effect of synthesis route on the structural, optical and magnetic properties of Fe3O4 nanoparticles, Ceram. Int. 40 (2014) 1945–1949.
[7] X. Gong, G. Liu, Y. Li, D.Y.W. Yu, W.Y. Teoh, Functionalized-graphene composites: fabrication and applications in sustainable energy and environment, Chem. Mater. 26 (2016) 8082–8118.
[8] A. Bianco, H.-M. Cheng, T. Enoki, Y. Gogotsi, R.H. Hurt, N. Koratkar, T. Kyotani, M. Monthioux, C.R. Park, J.M.D. Tascon, J. Zhang, All in the graphene family – A recommended nomenclature for two-dimensional carbon materials, Carbon 65 (2013) 1–6.
[9] A. Nieto, D. Lahiri, A. Agarwal, Synthesis and properties of bulk graphene nanoplatelets consolidated by spark plasma sintering, Carbon 50 (2012) 4068–4077.
[10] A. Peigney, C. Laurent, E. Flahaut, R.R. Bacsa, A. Rousset, Specific surface area of carbon nanotubes and bundles of carbon nanotubes, Carbon 39 (2001) 507–514.
[11] S. Chowdhury, R. Balasubramanian, Graphene/semiconductor nanocomposites (GSNs) for heterogeneous photocatalytic decolorization of wastewaters contaminated with synthetic dyes: a review, Appl. Catal. B: Environ. 160–161 (2014) 307–324.
[12] A. Arshad, J. Iqbal, M. Siddiq, M.U. Ali, A. Ali, H. Shabbir, U.B. Nazeer, M. S. Saleem, Solar light triggered catalytic performance of graphene-CuO nanocomposite for waste water treatment, Ceram. Int. 43 (2017) 10654–10660.
[13] X. Li, J. Yu, S. Wageh, A.A. Al-Ghamdi, J. Xie, Graphene in photocatalysis: a review, Small 12 (2016) 6640–6696.
[14] R. Matos, M.S. Nunes, I. Kuźniarska-Biernacka, M. Rocha, A. Guedes, A.C. Estrada, J.L. Lopes, T. Trindade, C. Freire, Graphene@Metal sulfide/oxide nanocomposites as novel photo-fenton-like catalysts for 4-nitrophenol degradation, Eur. J. Inorg. Chem. 2021 (2021) 4915–4928.
[15] A.C. Estrada, F.M. Silva, S.F. Soares, J.A.P. Coutinho, T. Trindade, An ionic liquid route to prepare copper sulphide nanocrystals aiming at photocatalytic applications, RSC Adv. 6 (2016) 34521–34528.
[16] P.K. Boruah, B. Sharma, I. Karbhal, M.V. Shelke, M.R. Das, Ammonia-modified graphene sheets decorated with magnetic Fe3O4 nanoparticles for the photocatalytic and photo-Fenton degradation of phenolic compounds under sunlight irradiation, J. Hazard Mater. 325 (2017) 90–100.
[17] P. Wang, L. Wang, Q. Sun, S. Qiu, Y. Liu, X. Zhang, X. Liu, L. Zheng, Preparation and performance of Fe3O4@hydrophilic graphene composites with excellent Photo-Fenton activity for photocatalysis, Mater. Lett. 183 (2016) 61–64.
[18] P. Borthakur, P.K. Boruah, G. Darabdhara, P. Sengupta, M.R. Das, A.I. Boronin, L. S. Kibis, M.N. Kozlova, V.E. Fedorov, Microwave assisted synthesis of CuS-reduced graphene oxide nanocomposite with efficient photocatalytic activity towards azo dye degradation, J. Environ. Chem. Eng. 4 (2016) 4600–4611.
[19] P.K. Boruah, P. Borthakur, G. Darabdhara, C.K. Kamaja, I. Karbhal, M.V. Shelke, P. Phukan, D. Saikia, M.R. Das, Sunlight assisted degradation of dye molecules and reduction of toxic Cr(vi) in aqueous medium using magnetically recoverable Fe3O4/reduced graphene oxide nanocomposite, RSC Adv. 6 (2016) 11049–11063.
[20] S. Yu, J. Liu, W. Zhu, Z.-T. Hu, T.-T. Lim, X. Yan, Facile room-temperature synthesis of carboxylated graphene oxide-copper sulfide nanocomposite with high photodegradation and disinfection activities under solar light irradiation, Sci. Rep. 5 (2015) 16369.
[21] A. Arshad, J. Iqbal, I. Ahmad, M. Israr, Graphene/Fe3O4 nanocomposite: Interplay between photo-Fenton type reaction, and carbon purity for the removal of methyl orange, Ceram. Int. 44 (2018) 2643–2648.
[22] C. Pereira, A.M. Pereira, C. Fernandes, M. Rocha, R. Mendes, M.P. Fernández-García, A. Guedes, P.B. Tavares, J.-M. Grenèche, J.P. Araújo, C. Freire,

Superparamagnetic MFe2O4 (M = Fe, Co, Mn) nanoparticles: tuning the particle size and magnetic properties through a novel one-step coprecipitation route, Chem. Mater. 24 (2012) 1496–1504.
[23] S.C. Ngo, K.K. Banger, M.J. DelaRosa, P.J. Toscano, J.T. Welch, Thermal and structural characterization of a series of homoleptic Cu(II) dialkyldithiocarbamate complexes: bigger is only marginally better for potential MOCVD performance, Polyhedron 22 (2003) 1575–1583.
[24] J.L.E. Lopes, A.C, S. Fateixa, M. Ferro, T. Trindade, A general route for growing metal sulfides onto graphene oxide and exfoliated graphite oxide, Nanomaterials 7 (2017) 245.
[25] S.Handlingar Lagergren, Band 24 (1898) 1–39.
[26] Y.S. Ho, G. McKay, Pseudo-second order model for sorption processes, Process Biochem. 34 (1999) 451–465.
[27] W.H. Cheung, Y.S. Szeto, G. McKay, Intraparticle diffusion processes during acid dye adsorption onto chitosan, Bioresour. Technol. 98 (2007) 2897–2904.
[28] R.-S. Juang, M.-L. Chen, Application of the elovich equation to the kinetics of metal sorption with solvent-impregnated resins, Ind. Eng. Chem. Res. 36 (1997) 813–820.
[29] J. Zhang, R. Stanforth, Slow adsorption reaction between arsenic species and goethite (α-FeOOH): diffusion or heterogeneous surface reaction control, Langmuir 21 (2005) 2895–2901.
[30] A. Bhatnagar, A.K. Jain, A comparative adsorption study with different industrial wastes as adsorbents for the removal of cationic dyes from water, J. Colloid Interface Sci. 281 (2005) 49–55.
[31] N.Y. Mezenner, A. Bensmaili, Kinetics and thermodynamic study of phosphate adsorption on iron hydroxide-eggshell waste, Chem. Eng. J. 147 (2009) 87–96.
[32] N. Suriyanon, P. Punyapalakul, C. Ngamcharussrivichai, Mechanistic study of diclofenac and carbamazepine adsorption on functionalized silica-based porous materials, Chem. Eng. J. 214 (2013) 208–218.
[33] G.E. Boyd, A.W. Adamson, L.S. Myers, The exchange adsorption of ions from aqueous solutions by organic zeolites. II. Kinetics1, J. Am. Chem. Soc. 69 (1947) 2836–2848.
[34] J.I. Paredes, M. Burghard, A. Martínez-Alonso, J.M.D. Tascón, Graphitization of carbon nanofibers: visualizing the structural evolution on the nanometer and atomic scales by scanning tunneling microscopy, Appl. Phys. A 80 (2005) 675–682.
[35] N. Sreelekha, K. Subramanyam, D. Amaranatha Reddy, G. Murali, S. Ramu, K. Rahul Varma, R.P. Vijayalakshmi, Structural, optical, magnetic and photocatalytic properties of Co doped CuS diluted magnetic semiconductor nanoparticles, Appl. Surf. Sci. 378 (2016) 330–340.
[36] Crystallography Open Database COD, h. w. c. n.
[37] J. Zhou, H. Song, L. Ma, X. Chen, Magnetite/graphene nanosheet composites: interfacial interaction and its impact on the durable high-rate performance in lithium-ion batteries, RSC Adv. 1 (2011) 782–791.
[38] Powder Diffraction: Theory and Practice, e. R. E. D.; and S. J. L. Billinge, R. P., Cambridge, UK,. 2008.
[39] S. Alwarappan, K. Cissell, S. Dixit, C.-Z. Li, S. Mohapatra, Chitosan-modified graphene electrodes for DNA mutation analysis, J. Electroanal. Chem. 686 (2012) 69–72.
[40] S. Sun, Y. Cao, J. Feng, P. Wu, Click chemistry as a route for the immobilization of well-defined polystyrene onto graphene sheets, J. Mater. Chem. 20 (2010) 5605–5607.
[41] D. Geng, S. Yang, Y. Zhang, J. Yang, J. Liu, R. Li, T.-K. Sham, X. Sun, S. Ye, S. Knights, Nitrogen doping effects on the structure of graphene, Appl. Surf. Sci. 257 (2011) 9193–9198.
[42] Y. Lu, F. Zhang, T. Zhang, K. Leng, L. Zhang, X. Yang, Y. Ma, Y. Huang, M. Zhang, Y. Chen, Synthesis and supercapacitor performance studies of N-doped graphene materials using o-phenylenediamine as the double-N precursor, Carbon 63 (2013) 508–516.
[43] W. Gao, G. Wu, M.T. Janicke, D.A. Cullen, R. Mukundan, J.K. Baldwin, E.L. Brosha, C. Galande, P.M. Ajayan, K.L. More, A.M. Dattelbaum, P. Zelenay, Ozonated graphene oxide film as a proton-exchange membrane, Angew. Chem. Int. Ed. 53 (2014) 3588–3593.
[44] S.K. Yadav, J.W. Cho, Functionalized graphene nanoplatelets for enhanced mechanical and thermal properties of polyurethane nanocomposites, Appl. Surf. Sci. 266 (2013) 360–367.
[45] K. Krishnamoorthy, M. Veerapandian, K. Yun, S.J. Kim, The chemical and structural analysis of graphene oxide with different degrees of oxidation, Carbon 53 (2013) 38–49.
[46] C.K. Chua, M. Pumera, Regeneration of a conjugated sp2 graphene system through selective defunctionalization of epoxides by using a proven synthetic chemistry mechanism, Chem. Eur. J. 20 (2014) 1871–1877.
[47] V.H. Pham, T.V. Cuong, S.H. Hur, E. Oh, E.J. Kim, E.W. Shin, J.S. Chung, Chemical functionalization of graphene sheets by solvothermal reduction of a graphene oxide suspension in N-methyl-2-pyrrolidone, J. Mater. Chem. 21 (2011) 3371–3377.
[48] N. Sreelekha, K. Subramanyam, D. Amaranatha Reddy, G. Murali, K. Rahul Varma, R.P. Vijayalakshmi, Efficient photocatalytic degradation of rhodamine-B by Fe doped CuS diluted magnetic semiconductor nanoparticles under the simulated sunlight irradiation, Solid State Sci. 62 (2016) 71–81.
[49] S. Askari, H. Koolivand, M. Pourkhalil, R. Lotfi, A. Rashidi, Investigation of Fe3O4/Graphene nanohybrid heat transfer properties: experimental approach, Int. Commun. Heat. Mass Transf. 87 (2017) 30–39.
[50] G. Wang, T. Liu, X. Xie, Z. Ren, J. Bai, H. Wang, Structure and electrochemical performance of Fe3O4/graphene nanocomposite as anode material for lithium-ion batteries, Mater. Chem. Phys. 128 (2011) 336–340.
[51] Y. Ren, H. Wei, B. Yang, J. Wang, J. Ding, "Double-Sandwich-Like" CuS@reduced graphene oxide as an Anode in Lithium Ion Batteries with Enhanced Electrochemical Performance, Electrochim. Acta 145 (2014) 193–200.
[52] X. Li, K. Zhou, J. Zhou, J. Shen, M. Ye, CuS nanoplatelets arrays grown on graphene nanosheets as advanced electrode materials for supercapacitor applications, J. Mater. Sci. Technol. 34 (2018) 2342–2349.
[53] T. Hurma, S. Kose, XRD Raman analysis and optical properties of CuS nanostructured film, Optik 127 (2016) 6000–6006.
[54] X. Fu, G. Yang, J. Sun, J. Zhou, Vibrational spectra of copper sulfate hydrates investigated with low-temperature raman spectroscopy and terahertz time domain spectroscopy, J. Phys. Chem. A 116 (2012) 7314–7318.
[55] G.V.M. Jacintho, A.G. Brolo, P. Corio, P.A.Z. Suarez, J.C. Rubim, Structural investigation of MFe2O4 (M = Fe, Co) magnetic fluids, J. Phys. Chem. C. 113 (2009) 7684–7691.
[56] A. Mezni, I. Balti, A. Mlayah, N. Jouini, L.S. Smiri, Hybrid Au–Fe3O4 nanoparticles: plasmonic, surface enhanced raman scattering, and phase transition properties, J. Phys. Chem. C. 117 (2013) 16166–16174.
[57] I. Chamritski, G. Burns, Infrared- and raman-active phonons of magnetite, maghemite, and hematite: a computer simulation and spectroscopic study, J. Phys. Chem. B 109 (2005) 4965–4968.
[58] Y.-S. Li, J.S. Church, A.L. Woodhead, Infrared and Raman spectroscopic studies on iron oxide magnetic nano-particles and their surface modifications, J. Magn. Magn. Mater. 324 (2012) 1543–1550.
[59] S.W. d Silva, T.F.O. Melo, M.A.G. Soler, E.C.D. Lima, M.F. d Silva, P.C. Morais, Stability of citrate-coated magnetite and cobalt-ferrite nanoparticles under laser irradiation: a Raman spectroscopy investigation, IEEE Trans. Magn. 39 (2003) 2645–2647.
[60] H. Wu, G. Wu, L. Wang, Peculiar porous α-Fe2O3, γ-Fe2O3 and Fe3O4 nanospheres: facile synthesis and electromagnetic properties, Powder Technol. 269 (2015) 443–451.
[61] M.M. Barsan, I.S. Butler, J. Fitzpatrick, D.F.R. Gilson, High-pressure studies of the micro-Raman spectra of iron cyanide complexes: Prussian blue (Fe4[Fe(CN)6]3), potassium ferricyanide (K3[Fe(CN)6]), and sodium nitroprusside (Na2[Fe(CN)5(NO)]·2H2O), J. Raman Spectrosc. 42 (2011) 1820–1824.
[62] A. Johansson, H.-C. Tsai, J. Aumanen, J. Koivistoinen, P. Myllyperkiö, Y.-Z. Hung, M.-C. Chuang, C.-H. Chen, W.Y. Woon, M. Pettersson, Chemical composition of two-photon oxidized graphene, Carbon 115 (2017) 77–82.
[63] Y. Wang, K. Huang, A. Derré, P. Puech, S. Rouzière, P. Launois, C. Castro, M. Monthioux, A. Pénicaud, Conductive graphene coatings synthesized from graphenide solutions, Carbon 121 (2017) 217–225.
[64] M. Seredych, E. Rodríguez-Castellón, M.J. Biggs, W. Skinner, T.J. Bandosz, Effect of visible light and electrode wetting on the capacitive performance of S- and N-doped nanoporous carbons: importance of surface chemistry, Carbon 78 (2014) 540–558.
[65] S.K. Chawla, N. Sankarraman, J.H. Payer, Diagnostic spectra for XPS analysis of Cu O S H compounds, J. Electron Spectrosc. Relat. Phenom. 61 (1992) 1–18.
[66] L. Mikyung, Y. Kijung, Highly efficient visible light photocatalysis of novel CuS/ZnO heterostructure nanowire arrays, Nanotechnology 23 (2012), 194014.
[67] V. Krylova, Optical, XPS and XRD Studies of Semiconducting Copper Sulfide Layers on a Polyamide Film, Int. J. Photo (2009) *2009*.
[68] C. Combellas, M. Delamar, F. Kanoufi, J. Pinson, F.I. Podvorica, Spontaneous grafting of iron surfaces by reduction of aryldiazonium salts in acidic or neutral aqueous solution. application to the protection of iron against corrosion, Chem. Mater. 17 (2005) 3968–3975.
[69] N.A. Eltouny, P.A. Ariya, Fe3O4 nanoparticles and carboxymethyl cellulose: a green option for the removal of atmospheric benzene, toluene, ethylbenzene, and o-Xylene (BTEX), Ind. Eng. Chem. Res. 51 (2012) 12787–12795.
[70] I.A.W. Tan, A.L. Ahmad, B.H. Hameed, Adsorption isotherms, kinetics, thermodynamics and desorption studies of 2,4,6-trichlorophenol on oil palm empty fruit bunch-based activated carbon, J. Hazard Mater. 164 (2009) 473–482.
[71] H. Ge, C. Wang, S. Liu, Z. Huang, Synthesis of citric acid functionalized magnetic graphene oxide coated corn straw for methylene blue adsorption, Bioresour. Technol. 221 (2016) 419–429.
[72] S. Nethaji, A. Sivasamy, A.B. Mandal, Adsorption isotherms, kinetics and mechanism for the adsorption of cationic and anionic dyes onto carbonaceous particles prepared from Juglans regia shell biomass, Int. J. Environ. Sci. Technol. 10 (2013) 231–242.
[73] K. Liu, H. Li, Y. Wang, X. Gou, Y. Duan, Adsorption and removal of rhodamine B from aqueous solution by tannic acid functionalized graphene, Colloids Surf. A: Physicochem. Eng. Asp. 477 (2015) 35–41.
[74] Z. Wu, X. Yuan, H. Zhong, H. Wang, L. Jiang, L. Leng, H. Wang, G. Zeng, Z. Liu, Effective removal of high-chroma rhodamine B over Sn0.215In0.38S/reduced graphene oxide composite: synergistic factors and mechanism of adsorption enrichment and visible photocatalytic degradation, Powder Technol. 329 (2018) 217–231.
[75] K.Y. Foo, B.H. Hameed, Textural porosity, surface chemistry and adsorptive properties of durian shell derived activated carbon prepared by microwave assisted NaOH activation, Chem. Eng. J. 187 (2012) 53–62.
[76] X. Hu, Y. Zhao, H. Wang, X. Tan, Y. Yang, Y. Liu, Efficient removal of tetracycline from aqueous media with a Fe3O4 nanoparticles@graphene oxide nanosheets assembly, Int. J. Environ. Res. Public Health 14 (2017).

[77] N. Liu, W. Huang, X. Zhang, L. Tang, L. Wang, Y. Wang, M. Wu, Ultrathin graphene oxide encapsulated in uniform MIL-88A(Fe) for enhanced visible light-driven photodegradation of RhB, Appl. Catal. B: Environ. 221 (2018) 119–128.
[78] J.-J. Zhang, P. Qi, J. Li, X.-C. Zheng, P. Liu, X.-X. Guan, G.-P. Zheng, Three-dimensional Fe2O3–TiO2–graphene aerogel nanocomposites with enhanced adsorption and visible light-driven photocatalytic performance in the removal of RhB dyes, J. Ind. Eng. Chem. 61 (2018) 407–415.
[79] Y. Cui, S.M. Goldup, S. Dunn, Photodegradation of Rhodamine B over Ag modified ferroelectric BaTiO3 under simulated solar light: pathways and mechanism, RSC Adv. 5 (2015) 30372–30379.